Detailed nucleation process and mechanism of the July 2019 Mw 6.4 Ridgecrest, California earthquake

Min Liu[1,2,3], Miao Zhang[2*] and Hongyi Li[1*,3]

[1]School of Geophysics and Information Technology, China University of Geosciences (Beijing), Beijing, China

[2]Department of Earth and Environmental Sciences, Dalhousie University, Halifax, Nova Scotia, Canada

[3]Shanghai Sheshan National Geophysical Observatory, Shanghai, China

Corresponding author: Miao Zhang (miao.zhang@dal.ca) and Hongyi Li (lih@cugb.edu.cn)

Key points:

- We detected and located 40 foreshocks of the July 2019 Mw 6.4 Ridgecrest earthquake using the Match&Locate method.
- The detailed spatiotemporal evolution of the foreshocks outlines a complex fault system accommodating the nucleation of the Mw 6.4 mainshock.
- The nucleation of the Mw 6.4 earthquake can be prominently explained by the cascade triggering model.

Abstract

Foreshocks provide valuable information on the nucleation process and mechanism of impending earthquakes. In this study, we utilized the Match&Locate method to build a high-precision foreshock catalog for the July 2019 Mw 6.4 Ridgecrest, California earthquake. The Mw 6.4 mainshock was preceded by 40 foreshocks within ~2 hours (on July 4, 2017 from 15:35:29 to 17:32:52, UTC). Their spatiotemporal distribution reveals a complex seismogenic structure consisting of multiple fault strands, which were connected as a throughgoing fault by later foreshocks and eventually accommodated the 2019 Mw 6.4 mainshock. To better understand the nucleation mechanism, we conducted a series of analysis for the foreshocks including repeating earthquake identification, rupture directivity inversion, and Coulomb stress change estimation. We identified a pair of small earthquakes with close magnitude, high waveform similarity, and high cross-spectral coherence at the early nucleation stage. However, we cannot confirm if they are repeating earthquakes due to their low magnitude and insufficient sampling rate. Thus, the initial nucleartion mechanism is unclear to us. Following the largest M_L 4.0 foreshock, we found the majority of its aftershocks and the Mw 6.4 mainshock occurred within regions of increasing Coulomb stress, indicating that they were triggered by stress transfer. Our study suggests that the nucleation of the Mw 6.4 mainshock can be prominently explained by cascade triggering even though we cannot exclude the possible existence of a minor aseismic slip process at the early stage.

Plain Language Summary

The 2019 Mw 6.4 Ridgecrest, California earthquake was preceded by a significant foreshock sequence in the ~2 h leading up to the main shock, presenting a question: what is the relationship between the Mw 6.4 mainshock and its foreshocks? In this study, we comprehensively analyzed seismograms obtained from nine nearby stations before the Mw 6.4 earthquake using state-of-the-art methods. Our unprecedented high-precision earthquake catalog demonstrates the detailed spatiotemporal evolution of the foreshocks. We also investigated the nucleation mechanism of the Mw 6.4 and its foreshocks utilizing various methods. Our study suggests that stress transfer dominates the nucleation mechanism of the Mw 6.4 mainshock even though that we cannot exclude the existence of a minor aseismic slip process at the early stage.

1 Introduction

The July 2019 Ridgecrest earthquake sequence broke a nearly 20-year absence of strong earthquakes in southern California. This sequence included two closely-spaced (about 10 km apart; Figure 1) mainshocks: an Mw 6.4 event on 4 July, 2019 (at 17:33:49 UTC) and an Mw 7.1 event on 6 July 2019 (at 03:19:53 UTC). The two mainshocks activated a complex fault network, consisting of the main NW-trending fault with about 65 km surface rupture, the NE-trending cross fault with 15 km surface rupture, as well as multiple near-orthogonal buried faults which cut through the main fault (Figure 1) (Huang et al., 2020; Lin, 2020; Liu et al., 2020; Ross et al., 2019; Shelly, 2020). The Southern California Seismic Network (SCSN) reported 9 foreshocks in ~2 hours preceding the Mw 6.4 mainshock. Although the foreshock catalog has been further improved using state-of-the-art techniques, such as the template matching technique (Ross et al., 2019; Shelly, 2020) and a machine-learning-based phase picker (Liu et al., 2020), the relationship between the Mw 6.4 mainshock and its foreshocks (i.e., nucleation mechanism) is not well understood.

Two opposing models have been proposed to explain earthquake nucleation: the preslip model and the cascade model (Beroza & Ellsworth, 1996; Dodge et al., 1996; Ellsworth & Beroza, 1995; Mignan, 2014). In the preslip model, foreshocks are attributed to aseismic slip surrounding the eventual mainshock hypocenter and may appear as repeating earthquakes. This model provides the possibility for earthquake prediction (Bouchon et al., 2011; Chen and Shearer, 2013; Dodge et al., 1996; Kato et al., 2012; McGuire et al., 2005; Savage et al., 2017; Tape et al.,. 2018). In the cascade model, later earthquakes usually occur in regions of increasing stress, which are imparted by adjacently preceding events (Ellsworth & Bulut, 2018; Felzer et al., 2004; Helmstetter & Sornette, 2003; Yoon et al., 2019). In other words, under this model, earthquakes, even the large ones, are random outcomes of triggering, implying that earthquake prediction is impossible (Ellsworth & Beroza, 1995). Recently, a combination of both mechanisms has been proposed to understand the complex nucleation process of some moderate-large earthquakes (Durand et al., 2020; Savage et al., 2017; Yao et al., 2020).

A comprehensive and high-precision earthquake catalog plays a key role in understanding the underlying earthquake nucleation mechanism. Using a matched filter is a promising technique for small earthquake detection, and involves the application of cross-correlation (CC) between the template events and continuous waveforms (Gibbons & Ringdal, 2006). Because this process assumes that the newly detected earthquakes are co-located with template events, the matched filter is only capable of detecting closely adjacent earthquakes and cannot provide specific location information. Thus, earthquakes have to be relocated separately using sequential algorithms such as cross-correlation and double-difference relocation (e.g., Ellsworth & Bulut, 2018; Yao et al., 2020; Yoon et al., 2019). Each of the above steps may affect the final earthquake catalog, from magnitude completeness to location accuracy. For instance, cross-correlation differential travel times are only maintained for waveform pairs with high similarity (e.g., CC > 0.7), which potentially decreases the number of available template phases/stations and reduces constraint for location. To solve this issue, Zhang and Wen (2015a) developed the Match&Locate method (M&L) to simultaneously detect and locate earthquakes, using all available components and stations, by maximizing the stacked waveform coherence based on the delay-and-sum concept. One remarkable application of this method was the detection and location of a controversial low-yield nuclear test conducted by North Korea in 2010 (Zhang & Wen, 2015b).

To understand the nucleation mechanism of the July 2019 Mw 6.4 Ridgecrest mainshock, we comprehensively investigated the relationship between the Mw 6.4 mainshock and its foreshocks. By applying the M&L method, we built a comprehensive and high-precision foreshock catalog. We utilized a novel rupture directivity analysis to estimate the rupture dimensions for the largest M_L 4.0 foreshock and adopted repeating earthquake identification and Coulomb stress change estimation to investigate the nucleation mechanism.

2 Detailed spatiotemporal evolution of foreshocks

We used the M&L method to detect and locate earthquakes before the Mw 6.4 mainshock. The target time range is about 2 hours preceding the Mw 6.4 mainshock from 15:35:26 to 17:32:52, UTC on July 4, 2019 (e.g., Liu et al., 2020; Shelly, 2020). Continuous seismic data were

collected from nine permanent stations within 60 km of the Mw 6.4 mainshock (Figure 1). We selected the M_L 1.5 foreshock as the template event (EQ 6; origin time: 16:13:43, UTC on July 4, 2019; see Table S1 in the supporting information), as it had a moderate magnitude with high signal-to-noise ratio and relatively high similarity to other SCSN cataloged foreshocks (Figure S1). The location of the template event was extracted from the CC hypoDD catalog (Shelly, 2020).

To efficiently conduct the M&L method, we built the foreshock catalog in two steps. The first step involved detecting and roughly locating earthquakes from continuous waveforms, while the second step involved refining their locations. In the first step, we searched for potential earthquakes within a 3D region centered at the template location: 0.006° × 0.006° × 600 m in longitude, latitude, and depth, with a searching interval of 0.0006° laterally (i.e., approximately 60 m) and 60 m vertically. Both P and S phases were utilized in the M&L method. We used the TauP software to calculate the theoretical P- and S-wave arrival times for the template event, as well as their horizontal and vertical slowness (Crotwell et al., 1999; Zhang and Wen, 2015a). The same 1-D velocity model suggested by Shelly (2020) was adopted. The template windows were 0.2 s before and 1.8 s after their theoretical arrival times. Such window settings enable us to separate P and S phases into corresponding time windows. We kept the default 100 Hz sampling interval for this step. We filtered the template and continuous waveforms from 2 to 12 Hz to improve the signal-to-noise ratio. With an empirical CC threshold of 0.35, we detected and located 39 foreshocks with magnitudes ranging from -0.39 to 4.0 (Figure 1; Table S1). Here, both location and magnitude were determined relative to the template event (see detailed method introduction in Zhang and Wen, 2015a). The second step focuses on refining the location of the events detected in the first step. To reduce calculation, waveforms of the 39 detected events were cut from 5 s before and 25 s after their origin time. The time window appropriately contains the entire earthquake signal at all stations. Earthquake locations were further refined within a smaller 3D region, with a finer search grid size centered at the optimal locations determined in the first step: 0.001° × 0.001° × 100 m in longitude, latitude, and depth with a searching interval of 0.00001° laterally (i.e., approximately 1 m) and 1 m vertically. To match this high spatial resolution, we interpolated the template and continuous waveforms from 100 to 5000 Hz. Finally, we detected and located 40 earthquakes with high precision (Figure 2). Waveform

comparison between these detections and the template event along with their CC spatial convergence verified the reliability and accuracy of their locations (Figure 3).

To quantify the location uncertainty, we adopted the widely used Jackknife method (Grigoli et al., 2013; Li et al., 2018, 2020; Waldhauser & Ellsworth, 2000). We repeatedly performed the aforementioned two-step M&L relocation 200 times and randomly removed three stations (33%) in each round. We determined the standard deviation of the 200 location errors of each event as its location uncertainty (Li et al., 2018). The results of the Jackknife analysis indicate that the average location uncertainties of these events are 10.5 m, 11 m and 28.9 m in the east, north and vertical direction, respectively.

We also compared our M&L catalog with the CC hypoDD catalog provided by Shelly (2020). All 35 events reported in the CC hypoDD catalog were recovered with the M&L method. Even though they are independently located with different algorithms and slightly different stations, the common events are consistent in space with an average hypocentral separation of 34.2 m, except for the 20190704T17:16:50 event (Figures 4). The slight hypocentral separation may be caused by three main reasons: 1) slightly different stations were used in the two catalogs. Compared with the CC hypoDD catalog, we include one more station in the NE direction (i.e., station SLA). 2) different inputs and algorithms are used in the two methods. The M&L locates earthquakes through maximizing the averaged CC coefficient among all components whereas the hypoDD minimizing travel time residual of those phase pairs with relatively large CC; 3) the M&L located these foreshocks based on the same template event, whereas the events in the hypoDD catalog were constrained by neighbor events including the aftershocks of the Mw 6.4 mainshock. To show waveform matching of the event with largest hypocentral difference between the two catalogs, we allocated corresponding hypocenters and origin times to the event, and compared its waveforms with the M_L 1.5 reference event after location correction (Figure 5). We observed the M&L catalog-based waveform matching is better than the CC hypoDD catalog (Figure 5), especially at the close stations (e.g., B921 and CLC), illuminating that our location is more reasonable and accurate.

This unprecedented high-precision catalog enables us to reveal detailed spatiotemporal migration of foreshocks and delineate the fine-scale structure of the fault zone (Figure 6 and Movie S1). On July 4, 2019 at 15:35:26 (UTC), a burst of small earthquakes began activating near the hypocenter of the Mw 6.4 mainshock (Figure 6a). After 45 min of silence, the largest M_L 4.0 foreshock nucleated nearby (Figure 6b). In the following 9 min, its early aftershocks occurred along a SW-dipping fault around its hypocenter (Figure 6b). Later on, a NW-trending shallow fault strand and a nearly north-trending deep low-dip fault strand were sequentially activated, and were gradually connected by later earthquakes before the occurrence of the Mw 6.4 mainshock, forming a throughgoing fault structure with a vertical length of 1.1 km (Figures 6c-d).

3 Rupture dimension analysis of the M_L 4.0 foreshock

Understanding rupture dimensions of foreshocks is essential to investigate their nucleation mechanism (Ellsworth & Bulut, 2018; Yao et al., 2020; Yoon et al., 2019). The largest M_L 4.0 foreshock cuts the 2-hour foreshock sequence into two segments and plays an important role in understanding the nucleation mechanism. Here we utilized a novel rupture directivity analysis to estimate its rupture direction and rupture radius. Based on the empirical Green's function method, similar to the relative directivity inversion method proposed by Xu and Wen (2019), we directly estimated the initial rupture point and centroid point of the M_L 4.0 earthquake using the M&L method. However, instead of minimizing the CC travel-time residual, the M&L method determines the two points by grid-searching the optimal location to maximize the averaged CC coefficient between the target event and the master event. Here, we kept the M_L 1.5 event as our master event because of its high signal-to-noise ratio, high similarity, and suitable magnitude. We utilized the initial P phases and full P and S phases to investigate the initial rupture point and centroid point, respectively. We used the same data processing techniques that were used to build the foreshock catalog. The centroid point was extracted directly from our high-precision foreshock catalog. In the initial point estimation, we set the template window as 0.03 s before and 0.03 s after the manually picked P-wave first arrival on the vertical component. The results indicate that the M_L 4.0 foreshock ruptured unilaterally along the NW fault with a rupture length of 630 m (i.e., twice the distance between the initial rupture point and centroid point), which is consistent with one of the reported nodal fault planes (SCSN; Figures 7a-b). Similarly, we determined the initial rupture point for the Mw 6.4 mainshock, which is located about 75 m SE of the master event (Figures 7c-d). Here, station SLA was not adopted due to the poor similarity between the Mw 6.4 event and the master event (Figure S2). The centroid point of the Mw 6.4 mainshock cannot be estimated in this way because it cannot be approximated by a point source model due to the large magnitude.

4 Nucleation of the Mw 6.4 mainshock and its foreshocks

We investigated whether the preslip model or cascade model could explain the nucleation mechanism of the Mw 6.4 mainshock. Repeating earthquakes (REs) occur on the same or overlapping fault areas (patch) and support the preslip model, but cannot be explained by the

cascade model (Ellsworth & Beroza, 1995). In other words, the existence of REs is an indicator of the preslip model. Thus, the identification of REs plays a critical role in distinguishing the two nucleation mechanisms.

In this study, we identified REs using three sequential criteria (Liu et al., 2019; Materna et al., 2018; Uchida, 2019; Uchida et al., 2009; Uchida & Bürgmann, 2019): 1) events must have similar magnitudes (< 0.5 unit); 2) events must have high waveform similarity at two or more stations (CC of any component > 0.95); 3) events must have high cross-spectral coherence at two or more stations (coherence of any component > 0.95). Since the majority of foreshocks have magnitude less than M_L 2.5, we adopted a high frequency range of 7-25 Hz to analyze their waveform similarity and cross-spectral coherence (Taira et al., 2014). Based on the three criteria, we selected a pair of candidate events (EQs 3 and 4) with a CC value larger than 0.95 at four stations (i.e., stations B917, B9121, CCC, and TOW2) and a cross-spectral coherence larger than 0.95 at two stations (i.e., stations B917 and B921) (Figures 8-9). The two events are separated by 7 m and 8 m in horizontal and vertical direction, respectively, potentially within the location uncertainty. Some stations have substandard CC values and/or cross-spectral coherence, which may be mainly caused by 1) low SNR due to large distance (e.g., station JRC2 and SLA; Figures 9d-i); 2) signal contamination by unknown noise (e.g., a signal of 25 Hz persistently exists at the station CLC). Thus, they are likely a pair of REs. However, according to Uchida (2019), the lower limit of analysis frequency of the EQ 3 (M_L 0.43) and EQ 4 (M_L 0.32) is beyond the Nyquist frequency (i.e., 50 Hz). It turns out that the current sampling rate is not high enough to confirm if they are REs with overlapping rupture. Similarly, we cannot utilize the spectral ratio method to estimate their source dimensions due to the insufficient sampling rate (Onwuemeka et al., 2018). According to Onwuemeka et al. 2018, a high sampling rate (~>250 Hz) would require to resolve the corner frequency of M <2 events. Thus, we are not able to distinguish which mechanism governs the early nucleation process. If the two events (EQs 3 and 4) are a pair of REs, it suggests that a minor aseismic slip process exists at the early stage of the nucleation process. Otherwise, it is also possible that the cascade triggering governs the nucleation process.

To investigate whether the cascade model can explain the late stage of the nucleation process, we analyzed the spatial relationship between foreshock hypocenters and nearby stress changes (Figure 10). We adopted two different approaches to estimate the stress change caused by the largest foreshock M_L 4.0 because it has available and reliable focal mechanism that required for stress change estimation. In the first approach, we calculated the Coulomb stress change according to the focal mechanism solution of the M_L 4.0 event (Lin & Stein, 2004). The initial rupture point of the M_L 4.0 foreshock estimated by the M&L method, one of the fault planes that matches rupture directivity (i.e., strike = 318°, rake = 167°, and dip = 81°; SCSN), and a recommended friction coefficient of 0.4 were adopted in the Coulomb stress change calculation (J. Lin & Stein, 2004; Toda et al., 2005). The majority of the aftershocks of the M_L 4.0 event, as well as the Mw 6.4 mainshock, nucleated in the regions with increasing Coulomb stress (Figures 10b-c), which suggested they were triggered by stress transfer. In the second approach, we empirically inferred the stress change imparted by the M_L4.0 event in space based on a simple circular crack (Kanamori & Anderson, 1975). From our previous directivity analysis, we know that the largest possible rupture radius of the M_L4.0 event is ~315 m (Figure 10a). Earthquakes following the M_L 4.0 earthquake as well as the Mw 6.4 mainshock, dominantly occurred outside of the rupture zone of the M_L 4.0 event (Figure 10a), where usually stress increases (Ellsworth & Bulut, 2018; Yoon et al., 2019). The two independent analyses suggest that the majority of aftershocks of the M_L 4.0 earthquake (84.3%) and Mw 6.4 mainshock were triggered by stress transfer, which is in line with the cascade model and consistent with the analysis of Ellsworth et al. (2020). We also noticed that a few earthquakes likely re-ruptured the source zone of the M_L 4.0 event (Figure 10a), which may be explained by aseismic slip or rupture heterogeneity (Ellsworth & Bulut, 2018).

Our observations show the majority of aftershocks of the M_L 4.0 earthquake, as well as the Mw 6.4 mainshock, were triggered by the stress change imparted by the M_L 4.0 event (Figures 10b-c). It is consistent with the analysis of Ellsworth et al. (2020), along with previous studies (Ellsworth & Bulut, 2018; Yao et al., 2020; Yoon et al., 2019), supporting that the cascade triggering controls earthquake nucleation. Whereas we cannot exclude the possibility that a minor aseismic slip ignited the nucleation process of the Mw 6.4 mainshock and cascade triggering predominantly governed the following.

5 Discussion

Immature fault systems that are transitioning into new major tectonic boundaries are usually characterized by a geometrically complex fault distribution and slow earthquake rupture (Crider & Peacock, 2004). Source inversion suggests that the Mw 6.4 and Mw 7.1 events ruptured with a slow velocity of about 1-2 km/s (Chen et al., 2020; Goldberg et al., 2020; Ross et al., 2019; Yang et al., 2020). Goldberg et al. (2020) concluded that the 2019 Ridgecrest sequence occurred on an immature fault. In this study, our foreshock catalog reveals a complex seismogenic structure, consisting of at least three fault strands with variable orientations (Figure 6), which independently supports the notion that the 2019 Ridgecrest sequence nucleated on an immature fault system. These individual fault strands are in fact small and may not be optimally oriented for large-scale earthquake failure (Crider & Peacock, 2004; Savage & Brodsky, 2011). However, a throughgoing fault structure was connected by the earthquakes following the Mw 4.0 event (Figure 6d), and accommodated the Mw 6.4 mainshock (Goldberg et al., 2020; Manighetti et al., 2007; Perrin et al., 2016; Thomas et al., 2013; Wesnousky, 1988).

Strain change provides the most direct evidence for the aseismic slip. But it is rarely observed in fields due to background noise effect. Ellsworth et al. (2020) estimated the lower limit of the observable strain at ~0.2 nanostrain between the M_L 4.0 foreshock and the Mw 6.4 mainshock, which is equivalent to an aseismic slip of Mw 3.5. Here we roughly estimated the accumulated moment magnitude for the pair of RE candidates (EQs 3 and 4) at Mw 0.95, which is much lower than the observable limit of Mw 3.5. Thus, we do not expect to observe the corresponding strain change even though a minor aseismic slip process exists.

Our observations suggest that the nucleation of the 2019 Mw 6.4 Ridgecrest mainshock can be prominently explained by the cascade model and in line with the previous studies (Ellsworth & Bulut, 2018; Yao et al., 2020; Yoon et al., 2019). However, we cannot exclude the possible existence of a minor aseismic slip at the very early state. In other words, it is possible that the Mw 6.4 event initiated the nucleation from a minor aseismic slip process and followed by

significant cascade triggering. Actually, the simultaneous existence of aseismic slip and cascade triggering during the nucleation process has been proposed in recent studies. Savage et al., (2017) utilized the hypoDD method to build a high-precision earthquake catalog for the Mw 5.0 earthquake sequence near Prague, OK, USA. They proposed that the aseismic slip and cascade triggering may co-exist during the sequence based on the hypocenter distribution and REs. Yao et al., (2020) comprehensively analyzed the foreshock sequence of the 2010 Mw 7.2 EI Mayor-Cucapah earthquake utilizing the template matching technique, relative location algorithm, and spectral ratio analysis. They speculated that the aseismic slip and stress transfer mechanisms may jointly contribute to the nucleation of the 2010 Mw 7.2 EI Mayor-Cucapah mainshock. Through analyzing the seismicity prior to the mainshock, Durand et al. (2020) suggested that a two-scale preparation phase governed the nucleation of the Mw 5.8 earthquake offshore Istanbul, Turkey: aseismic preparing the mainshock final rupture at first and following a cascade mechanism leading to the nucleation of the mainshock. Furthermore, laboratory experiments and numerical modeling also have implied the coalescence of the aseismic slip and transferred stress triggering during the earthquake nucleation (McLaskey, 2019; McLaskey & Lockner, 2014; Cattania & Segall, 2020; Dublanchet, 2018; Noda et al., 2013). Thus, the actual earthquake nucleation may be much more complicated than the two opposing nucleation models.

Previous studies usually apply the spectral ratio method to measure the rupture dimensions of earthquakes (Ellsworth & Bulut, 2018; Yao et al., 2020; Yoon et al., 2019). However, this method is limited by strict selection criteria of master events and empirical Green's functions (e.g., magnitude difference and close hypocenters). Besides, it only provides rupture size without rupture direction, which may affect our analysis of earthquake nucleation. In this study, we utilized the M&L method to directly measure the initial and centroid points of earthquake rupture (Figure 7), which can not only quantify the rupture size but also determine its rupture direction. Hence, our study also provides a new strategy to resolve the rupture dimension of earthquakes.

It is essential and critical to reliably and accurately estimate uncertainties of earthquake locations. However, there are no standard methods to estimate the location uncertainty that obtained with waveform-based methods (Li et al., 2020). In this study, we conducted a Jackknife

analysis to derive the statistical location uncertainty for all detections (Grigoli et al., 2013; Li et al., 2018, 2020; Waldhauser & Ellsworth, 2000). However, according to Waldhauser & Ellsworth (2000), the Jackknife analysis in fact mainly reflects the error due to improper station geometry, which may be about one order of magnitude smaller than the error caused by seismic data and velocity model.

6 Conclusions

We applied the M&L method to comprehensively investigate the detailed spatiotemporal evolution of the foreshocks preceding the Mw 6.4 earthquake. We cataloged 40 foreshocks that occurred ~2 h before the mainshock, with magnitudes ranging from −0.39 to 4.0. These foreshocks revealed a complex seismogenic structure, which accommodated the 2019 Mw 6.4 mainshock. To investigate the nucleation mechanism, we applied a series of analysis for the foreshocks including repeating earthquake identification, rupture directivity analysis, and Coulomb stress change estimation. At the early stage, we cannot distinguish either preslip or cascade model govens the nucleation process due to low magnitude of foreshocks and insufficient data sampling rate. Following the M_L 4.0 event, the majority of its aftershocks, and the Mw 6.4 earthquake, were triggered by stress transfer, suggesting a cascade triggering mechanism. Our study suggested that the nucleation of the Mw 6.4 mainshock can be prominently explained by the cascade model. Whereas we also cannot exclude the possibility that the nucleation initiated from a minor aseismic slip and followed by significant cascade triggering.

Acknowledgements

Waveform data were downloaded from the Incorporated Research Institutions for Seismology (http://ds.iris.edu/ds/nodes/dmc) and the Southern California Earthquake Data Center (https://scedc.caltech.edu/data/waveform.html). The hypoDD catalog can be accessed from Shelly (2020). Our foreshock catalog can be found in the supporting information. The M&L software is available through Zhang and Wen (2015a). The software used to analyze cross-spectral coherence was provide by Dongdong Yao. The maps in our paper were made using Generic Mapping Tools (Wessel et al., 2013), Python and MATLAB. We thank Katherine Scharer for sharing the surveyed surface ruptures. We thank William Ellsworth, David Shelly,

and Andrew Barbour for valuable comments on the first version of the manuscript. This work was co-supported by the National Natural Science Foundation of China (NSFC) under Grants U1939203 and 41874063, China Earthquake Science Experiment project, China Earthquake Administration (2019CSES0113), the Fundamental Research Funds for the Central Universities of China (2-9-2019-172), Shanghai Sheshan National Geophysical Observatory (No. 2020K02), and the Natural Sciences and Engineering Research Council of Canada Discovery Grant (RGPIN-2019-04297).

References

Abercrombie, R. E. (1996). The magnitude-frequency distribution of earthquakes recorded with deep seismometers at Cajon Pass, southern California. Tectonophysics, 261(1–3), 1–7. https://doi.org/10.1016/0040-1951(96)00052-2

Abercrombie, R. E. (2015). Investigating uncertainties in empirical Green's function analysis of earthquake source parameters. *Journal of Geophysical Research: Solid Earth*, *120*(6), 4263–4277. https://doi.org/10.1002/2015JB011984

Beroza, G. C., & Ellsworth, W. L. (1996). Properties of the seismic nucleation phase. *Tectonophysics*, *261*(1-3 SPEC. ISS.), 209–227. https://doi.org/10.1016/0040-1951(96)00067-4

Bouchon, M., Karabulut, H., Aktar, M., Özalaybey, S., Schmittbuhl, J., & Bouin, M. P. (2011). Extended nucleation of the 1999 Mw 7.6 Izmit earthquake. *Science*, *331*(6019), 877–880. https://doi.org/10.1126/science.1197341

Cattania, C., & Segall, P. (2020). Precursory slow slip and foreshocks on rough faults. https://doi.org/10.31223/osf.io/9xphk

Chen, K., Avouac, J. P., Aati, S., Milliner, C., Zheng, F., & Shi, C. (2020). Cascading and pulse-like ruptures during the 2019 Ridgecrest earthquakes in the Eastern California Shear Zone. *Nature Communications*, *11*(1), 3–10. https://doi.org/10.1038/s41467-019-13750-w

Crider, J. G., & Peacock, D. C. P. (2004). Initiation of brittle faults in the upper crust: A review of field observations. *Journal of Structural Geology*, *26*(4), 691–707. https://doi.org/10.1016/j.jsg.2003.07.007

Crotwell, H. P., Owens, T. J., & Ritsema, J. (1999). The TauP Toolkit: Flexible Seismic Travel-

time and Ray-path Utilities. *Seismological Research Letters*, *70*(2), 154–160. https://doi.org/10.1785/gssrl.70.2.154

Dodge, D. A., Beroza, G. C., & Ellsworth, W. L. (1996). Detailed observations of California foreshock sequences: Implications for the earthquake initiation process. *Journal of Geophysical Research: Solid Earth*, *101*(B10), 22371–22392. https://doi.org/10.1029/96jb02269

Dublanchet, P. (2018). The dynamics of earthquake precursors controlled by effective friction. *Geophysical Journal International*, *212*(2), 853–871. https://doi.org/10.1093/gji/ggx438

Durand, V., Bentz, S., Kwiatek, G., Dresen, G., Wollin, C., Heidbach, O., et al. (2020). A Two-Scale Preparation Phase Preceded an Mw 5.8 Earthquake in the Sea of Marmara Offshore Istanbul, Turkey. *Seismological Research Letters*. https://doi.org/10.1785/0220200110

Ellsworth, W. L., & Beroza, G. C. (1995). Seismic evidence for an earthquake nucleation phase. *Science*, *268*(5212), 851–855. https://doi.org/10.1126/science.268.5212.851

Ellsworth, William L., & Bulut, F. (2018). Nucleation of the 1999 Izmit earthquake by a triggered cascade of foreshocks. *Nature Geoscience*, *11*(7), 531–535. https://doi.org/10.1038/s41561-018-0145-1

Ellsworth, W. L., Barbour, A. J., & Shelly, D. R. (2020). Foreshock Cascade to Failure in the M 6.4 July 4, 2019 Ridgecrest, Califonia Earthquake. *JpGU-AGU Joint Meeting*.

Eshelby, J. D. (1957). The determination of the elastic field of an ellipsoidal inclusion, and related problems. *Proceedings of the Royal Society of London. Series A. Mathematical and Physical Sciences*, *241*(1226), 376–396. https://doi.org/10.1098/rspa.1957.0133

Felzer, K. R., Abercrombie, R. E., & Ekström, G. (2004). A common origin for aftershocks, foreshocks, and multiplets. *Bulletin of the Seismological Society of America*, *94*(1), 88–98. https://doi.org/10.1785/0120030069

Gibbons, S. J., & Ringdal, F. (2006). The detection of low magnitude seismic events using array-based waveform correlation. *Geophysical Journal International*, *165*(1), 149–166. https://doi.org/10.1111/j.1365-246X.2006.02865.x

Goldberg, D. E., Melgar, D., Sahakian, V. J., Thomas, A. M., Xu, X., Crowell, B. W., & Geng, J. (2020). Complex Rupture of an Immature Fault Zone: A Simultaneous Kinematic Model of the 2019 Ridgecrest, CA Earthquakes. *Geophysical Research Letters*, *47*(3), 0–2. https://doi.org/10.1029/2019GL086382

Grigoli, F., Cesca, S., Vassallo, M., & Dahm, T. (2013). Automated seismic event location by travel-time stacking: An application to mining induced seismicity. *Seismological Research Letters*, *84*(4), 666–677. https://doi.org/10.1785/0220120191

Helmstetter, A., & Sornette, D. (2003). Importance of direct and indirect triggered seismicity in the ETAS model of seismicity. *Geophysical Research Letters*, *30*(11), 1–4. https://doi.org/10.1029/2003GL017670

Huang, H., Meng, L., Bürgmann, R., Wang, W., & Wang, K. (2020). Spatio-temporal foreshock evolution of the 2019 M 6.4 and M 7.1 Ridgecrest, California earthquakes. *Earth and Planetary Science Letters*, *551*, 116582. https://doi.org/10.1016/j.epsl.2020.116582

Huang, Y., Beroza, G. C., & Ellsworth, W. L. (2016). Stress drop estimates of potentially induced earthquakes in the Guy-Greenbrier sequence. *Journal of Geophysical Research: Solid Earth*, *121*(9), 6597–6607. https://doi.org/10.1002/2016JB013067

Kanamori, H., & Anderson, D. L. (1975). Theoretical basis of some empirical relations in seismology. *Bulletin of the Seismological Society of America*, *65*(5), 1073–1095.

Kendrick, K. J., Akciz, S. O., Angster, S. J., Avouac, J., Bachhuber, J. L., Bennett, S. E., Blake, K., Bork, S., Brooks, B. A., Burgess, P., Chupik, C., Dawson, T., DeFrisco, M. J., Delano, J., DeLong, S., Dolan, J. F., DuRoss, C. B., Ericksen, T., Frost, M. E. (2019). Geologic observations of surface fault rupture associated with the Ridgecrest M6.4 and M7.1 earthquake sequence by the Ridgecrest Rupture Mapping Group. In *2019 SCEC Annual Meeting* (p. Poster #217).

Li, L., Becker, D., Chen, H., Wang, X., & Gajewski, D. (2018). A systematic analysis of correlation-based seismic location methods. *Geophysical Journal International*, *212*(1), 659–678. https://doi.org/10.1093/gji/ggx436

Li, L., Tan, J., Schwarz, B., Staněk, F., Poiata, N., Shi, P., et al. (2020). Recent advances and challenges of waveform‐based seismic location methods at multiple scales. *Reviews of Geophysics*, *58*(1), 1–47. https://doi.org/10.1029/2019RG000667

Lin, G. (2020). Waveform cross-correlation relocation and focal mechanisms for the 2019 ridgecrest earthquake sequence. *Seismological Research Letters*, *91*(4), 2055–2061. https://doi.org/10.1785/0220190277

Lin, J., & Stein, R. S. (2004). Stress triggering in thrust and subduction earthquakes and stress interaction between the southern San Andreas and nearby thrust and strike-slip faults.

Journal of Geophysical Research: Solid Earth, *109*(B2), 1–19. https://doi.org/10.1029/2003jb002607

Liu, M., Li, H., Peng, Z., Ouyang, L., Ma, Y., Ma, J., et al. (2019). Spatial-temporal distribution of early aftershocks following the 2016 Ms 6.4 Menyuan, Qinghai, China Earthquake. *Tectonophysics*, *766*, 469–479. https://doi.org/10.1016/j.tecto.2019.06.022

Liu, M., Zhang, M., Zhu, W., Ellsworth, W. L., & Li, H. (2020). Rapid Characterization of the July 2019 Ridgecrest, California, Earthquake Sequence From Raw Seismic Data Using Machine-Learning Phase Picker. *Geophysical Research Letters*, *47*(4), 1–9. https://doi.org/10.1029/2019GL086189

Madariaga, R. (1976). Bulletin of the Seismological Society of America . *Bulletin of the Seismological Society of America*, *66*(3). https://doi.org/10.1086/622062

Manighetti, I., Campillo, M., Bouley, S., & Cotton, F. (2007). Earthquake scaling, fault segmentation, and structural maturity. *Earth and Planetary Science Letters*, *253*(3–4), 429–438. https://doi.org/10.1016/j.epsl.2006.11.004

Materna, K., Taira, T., & Bürgmann, R. (2018). Aseismic Transform Fault Slip at the Mendocino Triple Junction From Characteristically Repeating Earthquakes. *Geophysical Research Letters*, *45*(2), 699–707. https://doi.org/10.1002/2017GL075899

McLaskey, G. C. (2019). Earthquake Initiation From Laboratory Observations and Implications for Foreshocks. *Journal of Geophysical Research: Solid Earth*, *124*(12), 12882–12904. https://doi.org/10.1029/2019JB018363

McLaskey, G. C., & Lockner, D. A. (2014). Preslip and cascade processes initiating laboratory stick slip. *Journal of Geophysical Research: Solid Earth*, *119*(8), 6323–6336. https://doi.org/10.1002/2014JB011220

Mignan, A. (2014). The debate on the prognostic value of earthquake foreshocks: A meta-analysis. *Scientific Reports*, *4*, 1–5. https://doi.org/10.1038/srep04099

Noda, H., Nakatani, M., & Hori, T. (2013). Large nucleation before large earthquakes is sometimes skipped due to cascade-up-Implications from a rate and state simulation of faults with hierarchical asperities. *Journal of Geophysical Research: Solid Earth*, *118*(6), 2924–2952. https://doi.org/10.1002/jgrb.50211

Onwuemeka, J., Liu, Y., & Harrington, R. M. (2018). Earthquake Stress Drop in the Charlevoix Seismic Zone, Eastern Canada. *Geophysical Research Letters*, *45*(22), 12,226-12,235.

https://doi.org/10.1029/2018GL079382

Perrin, C., Manighetti, I., Ampuero, J. P., Cappa, F., & Gaudemer, Y. (2016). Location of largest earthquake slip and fast rupture controlled by along-strike change in fault structural maturity due to fault growth. *Journal of Geophysical Research: Solid Earth*, *121*(5), 3666–3685. https://doi.org/10.1002/2015JB012671

Ross, Z. E., Idini, B., Jia, Z., Stephenson, O. L., Zhong, M., Wang, X., et al. (2019). Hierarchical interlocked orthogonal faulting in the 2019 Ridgecrest earthquake sequence. *Science*, *366*(6463), 346–351. https://doi.org/10.1126/science.aaz0109

Savage, H. M. & Brodsky, E. E. (2011). Collateral Damage: The evolution with displacement of fracture distribution and secondary fault strands in fault damage zones, *Journal of Geophysical Research: Solid Earth*, *116*(B3), doi:10.1029/2010JB007665

Savage, H. M., Keranen, K. M., P. Schaff, D., & Dieck, C. (2017). Possible precursory signals in damage zone foreshocks. *Geophysical Research Letters*, *44*(11), 5411–5417. https://doi.org/10.1002/2017GL073226

Shelly, D. R. (2020). A High-Resolution Seismic Catalog for the Initial 2019 Ridgecrest Earthquake Sequence: Foreshocks, Aftershocks, and Faulting Complexity. *Seismological Research Letters*. https://doi.org/10.1785/0220190309

Taira, T., Bürgmann, R., Nadeau, R. M., & Dreger, D. S. (2014). Variability of fault slip behavior along the San Andreas Fault in the San Juan Bautista Region. *Journal of Geophysical Research: Solid Earth*, *119*(12), 8827–8844. https://doi.org/10.1002/2014JB011427

Thomas, A. M., Bürgmann, R., & Dreger, D. S. (2013). Incipient faulting near lake pillsbury, california, and the role of: Accessory faults in plate boundary evolution. *Geology*, *41*(10), 1119–1122. https://doi.org/10.1130/G34588.1

Toda, S., Stein, R. S., Richards-Dinger, K., & Bozkurt, S. B. (2005). Forecasting the evolution of seismicity in southern California: Animations built on earthquake stress transfer. *Journal of Geophysical Research: Solid Earth*, *110*(5), 1–17. https://doi.org/10.1029/2004JB003415

Uchida, N. (2019). Detection of repeating earthquakes and their application in characterizing slow fault slip. *Progress in Earth and Planetary Science*, *6*(1). https://doi.org/10.1186/s40645-019-0284-z

Uchida, N., & Bürgmann, R. (2019). Repeating Earthquakes. *Annual Review of Earth and*

Planetary Sciences, *47*(May), 305–332. https://doi.org/10.1146/annurev-earth-053018-060119

Uchida, N., Nakajima, J., Hasegawa, A., & Matsuzawa, T. (2009). What controls interplate coupling?: Evidence for abrupt change in coupling across a border between two overlying plates in the NE Japan subduction zone. *Earth and Planetary Science Letters*, *283*(1–4), 111–121. https://doi.org/10.1016/j.epsl.2009.04.003

Uchida, N., Matsuzawa, T., Ellsworth, W. L., Imanishi, K., Shimamura, K., & Hasegawa, A. (2012). Source parameters of microearthquakes on an interplate asperity off Kamaishi, NE Japan over two earthquake cycles. *Geophysical Journal International*, *189*(2), 999–1014. https://doi.org/10.1111/j.1365-246X.2012.05377.x

Waldhauser, F., & Ellsworth, W. L. (2000). A Double-Difference Earthquake Location Algorithm: Method and Application to the Northern Hayward Fault, California. *Bulletin of the Seismological Society of America*, *90*(6), 1353–1368. https://doi.org/10.1785/0120000006

Wesnousky, S. G. (1988). Seismological and structural evolution of strike-slip faults. *Nature*. https://doi.org/10.1038/335340a0

Wessel, P., Smith, W. H. F., Scharroo, R., Luis, J., & Wobbe, F. (2013). Generic mapping tools: Improved version released. *Eos*, *94*(45), 409–410. https://doi.org/10.1002/2013EO450001

Xu, Y., & Wen, L. (2019). Relative directivity inversion of small earthquake rupture. *Geophysical Journal International*, *218*(1), 631–639. https://doi.org/10.1093/gji/ggz179

Yang, J., Zhu, H., & Lumley, D. (2020). Time−lapse imaging of coseismic ruptures for the 2019 Ridgecrest earthquakes using multi−azimuth back−projection with regional seismic data and a 3D crustal velocity model. *Geophysical Research Letters*, 1–18. https://doi.org/10.1029/2020gl087181

Yao, D., Huang, Y., Peng, Z., & Castro, R. R. (2020). Detailed Investigation of the Foreshock Sequence of the 2010 Mw 7.2 El Mayor−Cucapah Earthquake. *Journal of Geophysical Research: Solid Earth*, *9*(1), 76–99. https://doi.org/10.1029/2019JB019076

Yoon, C. E., Yoshimitsu, N., Ellsworth, W. L., & Beroza, G. C. (2019). Foreshocks and Mainshock Nucleation of the 1999 M w 7.1 Hector Mine, California, Earthquake. *Journal of Geophysical Research: Solid Earth*, *124*(2), 1569–1582. https://doi.org/10.1029/2018JB016383

Zhang, M., & Wen, L. (2015a). An effective method for small event detection: match and locate (M&L). *Geophysical Journal International*, *200*(3), 1523–1537. https://doi.org/10.1093/gji/ggu466

Zhang, M., & Wen, L. (2015b). Seismological evidence for a low-yield nuclear test on 12 May 2010 in North Korea. *Seismological Research Letters*, *86*(1), 138–145. https://doi.org/10.1785/02201401170

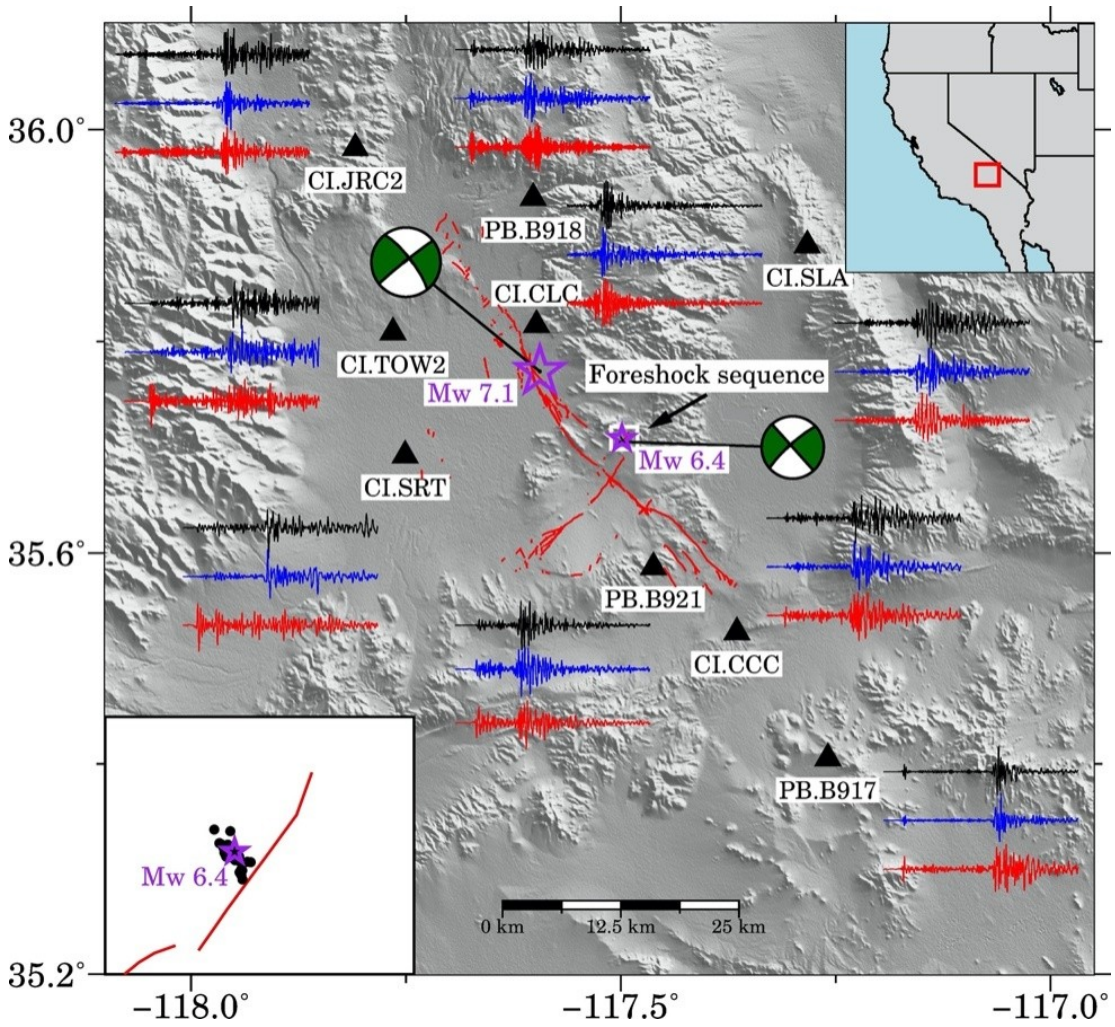

Figure 1. Map view of the study region. Epicenters and focal mechanisms of the Mw 6.4 and Mw 7.1 earthquakes are indicated by purple stars and beach balls, respectively. Black triangles denote the seismic stations used in this study. Red lines mark the surveyed surface ruptures (Kendrick et al., 2019). Three-component seismograms of the template M_L 1.5 event are plotted close to their corresponding stations. (bottom left inset) The 40 identified foreshocks, along with the Mw 6.4 mainshock, are shown in the zoomed-in area (white rectangle in main figure). The top-right displays a regional map of the United States, with the red rectangle indicating the study region.

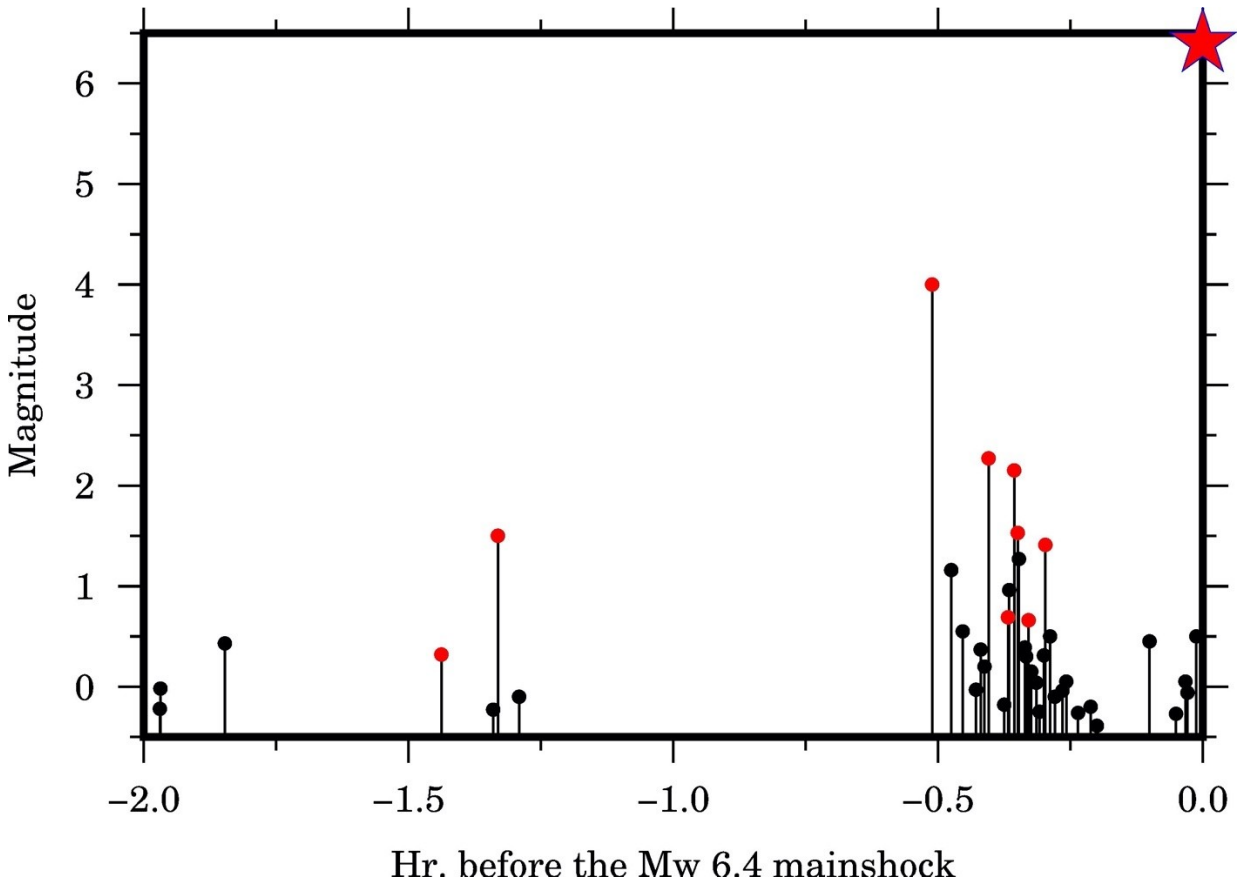

Figure 2. Magnitude-time distribution of the foreshocks in our M&L catalog (dots), along with the Mw 6.4 event (red star). Red dots indicate common events cataloged by the M&L and the SCSN.

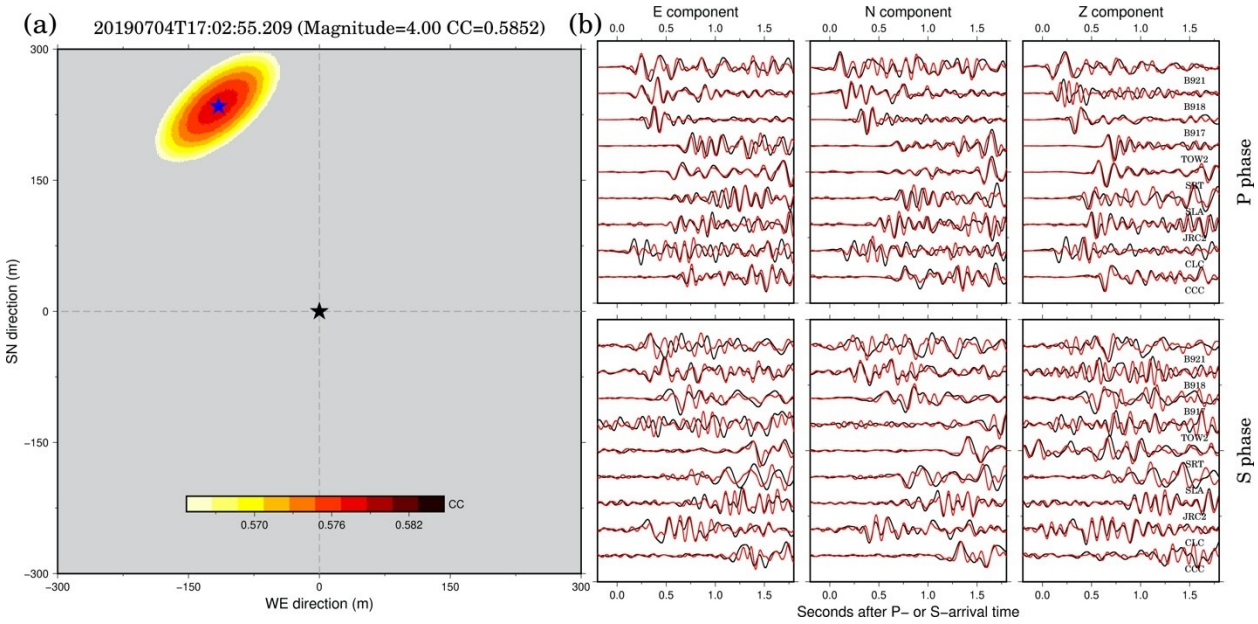

Figure 3. Horizontal CC convergence of the M_L 4.0 and its waveform comparison with the template event (M_L 1.5). (a) Black and blue stars represent the epicenters of the template and optimal location for the target event, respectively. The distribution of averaged CC coefficients is shown with a color bar. (b) Three-component waveform comparison of P phases (top panel) and S phases (bottom panel) between the M_L4.0 (red) and template (black) event after relative travel time correction. Similar analysis for other foreshocks can be found in Supporting Information.

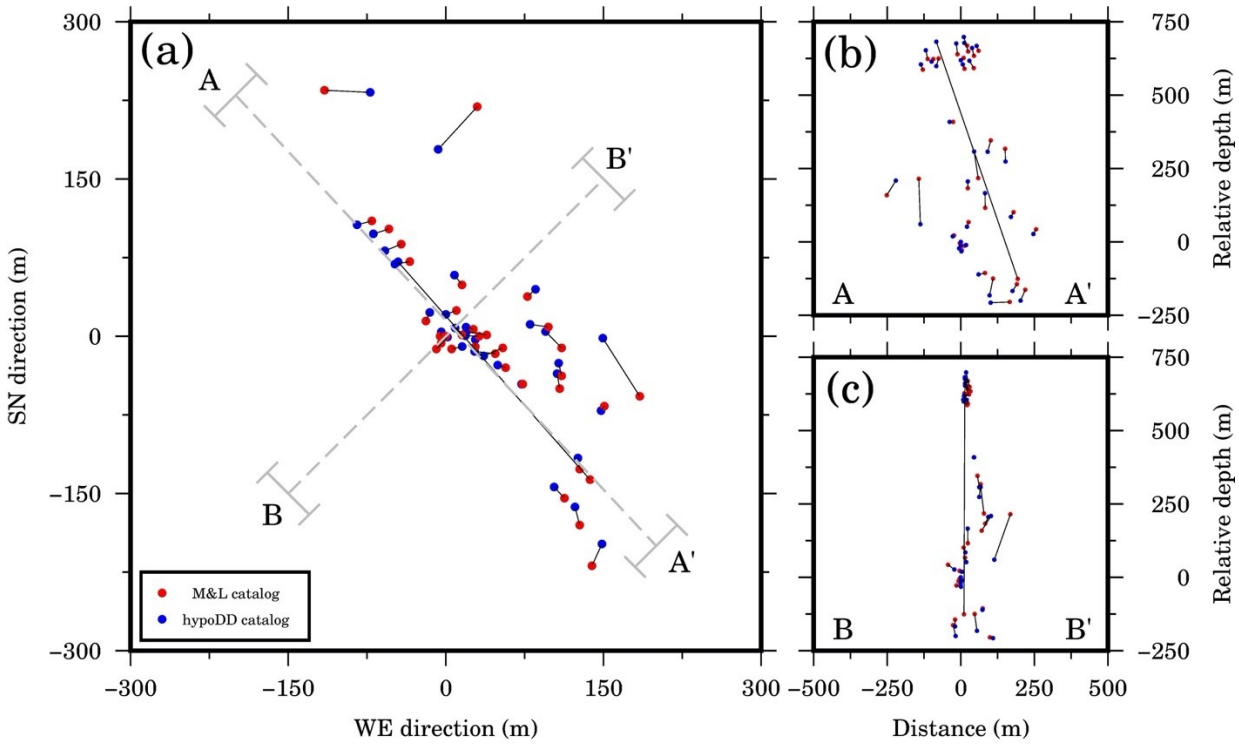

Figure 4. (a) Plane-view comparison of the 35 common foreshocks between the M&L catalog (red dots) and the CC hypoDD catalog (blue dots, from Shelly et al., 2020). Event locations are relative to the hypocenter of the M_L 1.5 event. The corresponding event-pairs in the two catalogs are connected by black lines. (b) Similar to (a), but for the cross-section along AA', which corresponds to one of the fault planes of the M_L 4.0 foreshock. (c) Similar to (b), but for the cross-section along BB'. The event-pair with the largest location difference is further analyzed in Figure 5.

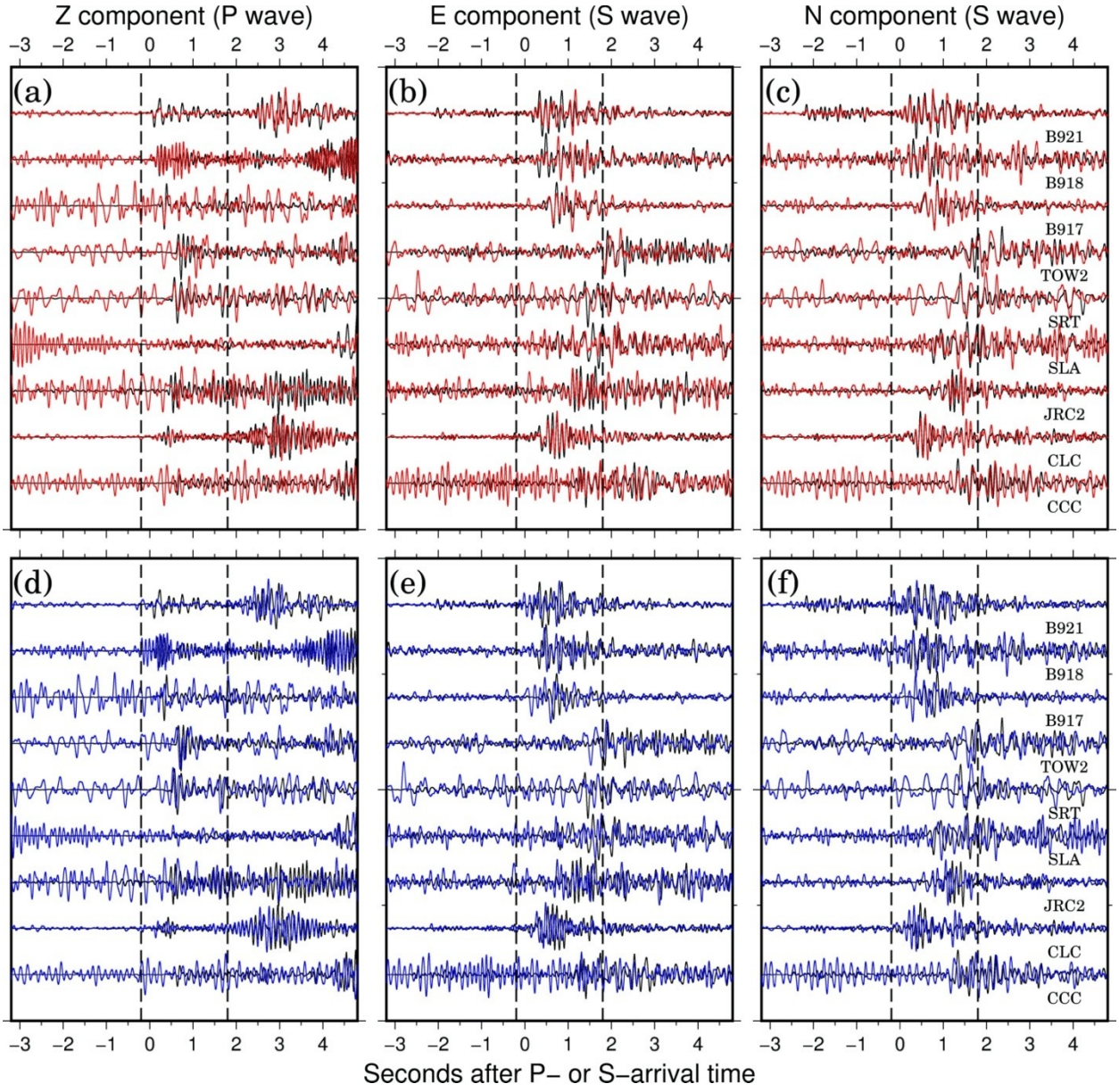

Figure 5. Investigation of the location reliability for the event pair with the largest location difference in Figure 4. We allocated the corresponding locations and origin times, listed in the M&L and hypoDD catalogs, to the target event, and compared its waveforms with the M_L 1.5 reference event after location correction. (a–c) Red and black waveforms represent the three-component seismograms of the event located by M&L and the reference event (M_L 1.5), respectively. Two black dashed lines highlight the template windows used in the M&L method. (d-f) Similar to (a–c), but for the CC hypoDD location.

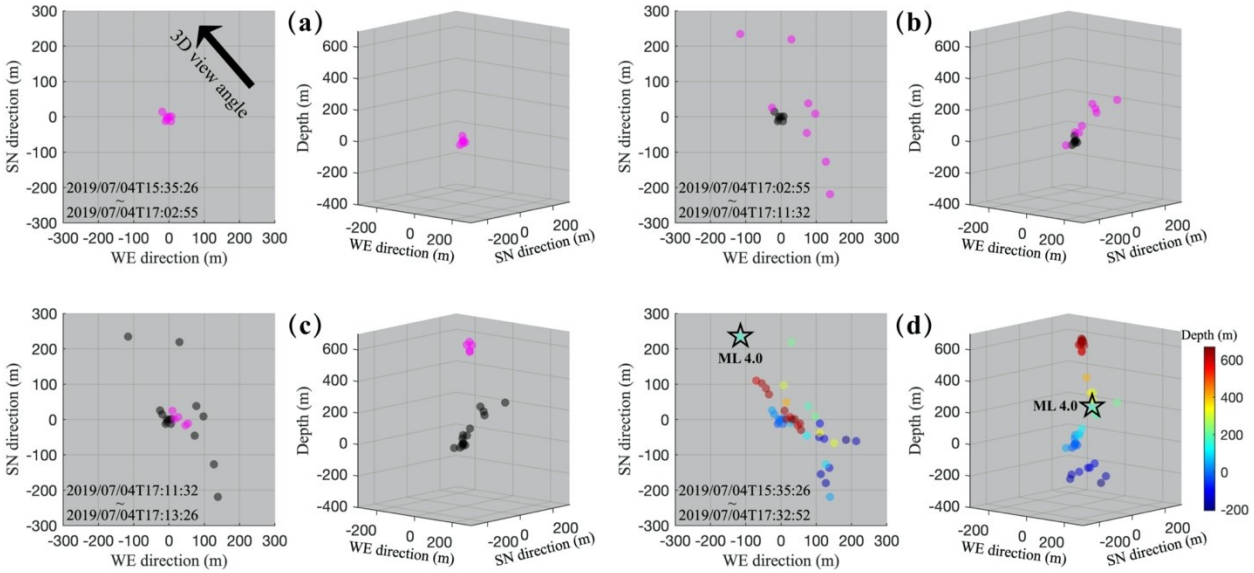

Figure 6. Detailed spatial-temporal evolution of foreshocks. (a) Left panel shows the map-view epicenters of foreshocks (purple dots) that occurred on July 4, 2019, from 15:35:25 to 17:02:55 (UTC; EQs 1-7). The right panel displays a 3D view, with a view angle indicated by the black arrow in the left panel. All event locations are relative to the hypocenter of the template event. (b) Similar to (a), but for the foreshocks that occurred from 17:02:55 to 17:11:32 (UTC; EQs 8-15). Black dots represent events that occurred within the previous time window. (c) Similar to (b), but for the foreshocks that occurred from 17:11:32 to 17:13:26 (UTC; EQs 16-20). (d) All foreshocks that occurred before the Mw 6.4 mainshock, colored by depth. Black star highlights the largest foreshock of M_L 4.0.

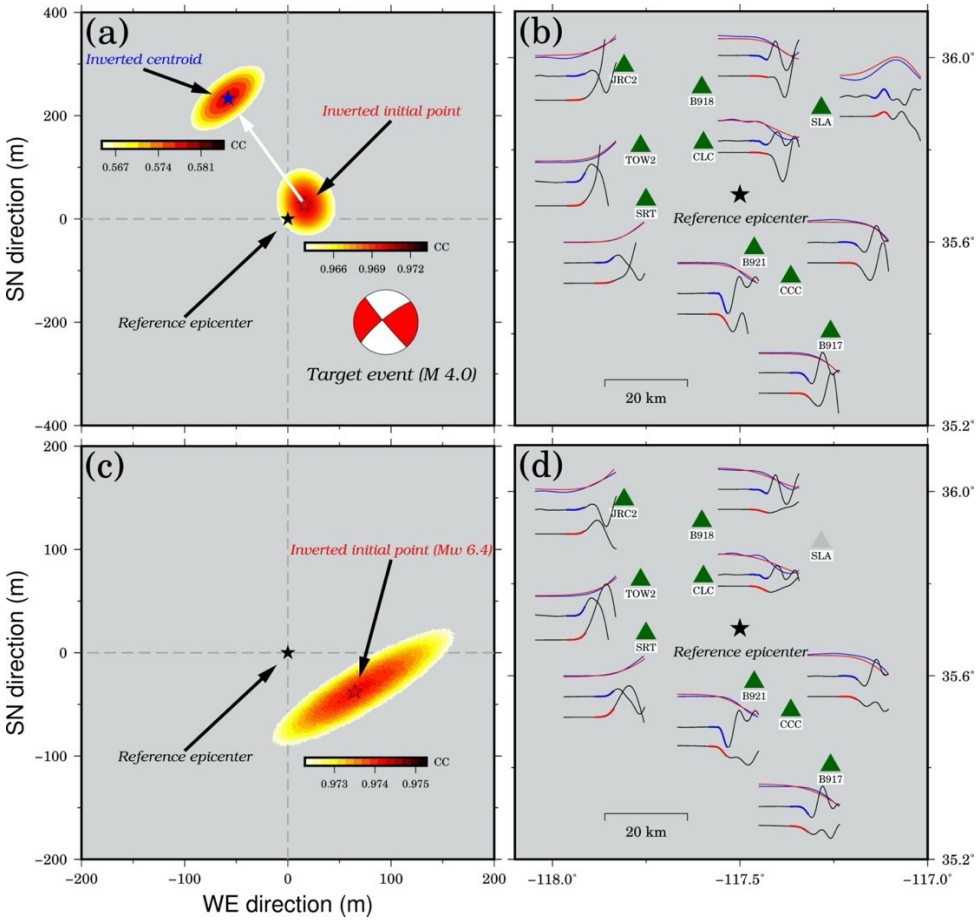

Figure 7. Rupture directivity analysis of the M_L 4.0 event and the initial rupture point of the Mw 6.4 mainshock determined by the M&L method. (a) Rupture directivity (white arrow) of the M_L 4.0 event. The black star indicates the epicenter of the reference event. Red and blue stars represent the initial rupture point and centroid point of the M_L 4.0 foreshock, respectively. The distributions of their averaged CC coefficients are shown with the corresponding color bars. Beach ball shows the focal mechanism solution of the M_L 4.0 event (SCSN). All locations are relative to the epicenter of the master event, in meters. (b) Initial P phase comparison between the M_L 4.0 event (red) and the M_L 1.5 reference event (blue) after travel time correction by M&L, which is used for the initial rupture point determination of the M_L 4.0 event. Initial P phases are plotted along with their early P phases over an extended time window (bottom two traces). Dark-green triangles represent the stations used for location determination by the M&L method. (c) Similar to (a), but for the initial rupture point determination of the Mw 6.4 mainshock. (d) Similar to (b), but for the initial rupture point determination of the Mw 6.4 mainshock. Gray triangle represents the discarded station.

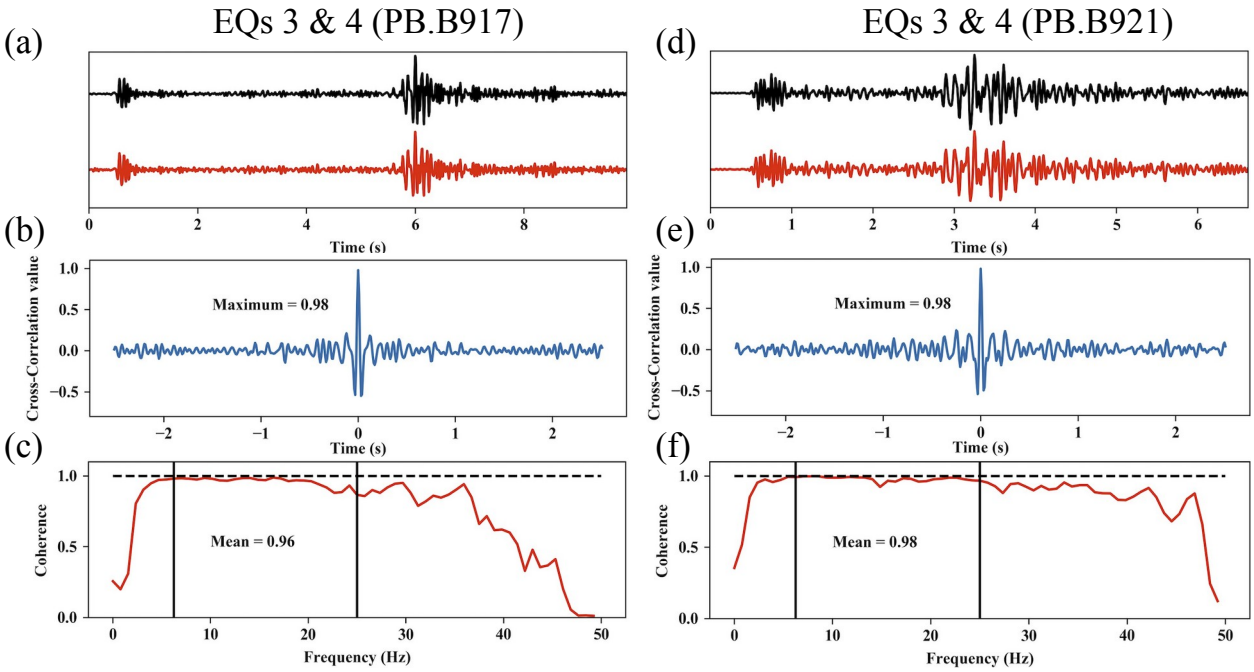

Figure 8. Waveform coherence analysis between the EQs 3 and 4. (a) Waveforms of the horizontal component (EH2) at station B917. Black and red traces are for the EQs 3 and 4, respectively. Waveforms were bandpass filtered in a frequency range of 7-25 Hz. (b) The cross-correlation function between the two waveforms in (a). (c) The coherence function between the two waveforms in (a). Two black lines mark the frequency band (i.e., 7-25 Hz) that used for the mean coherence calculation (i.e., 0.96). (d-f) Similar to (a-c), but for station B921.

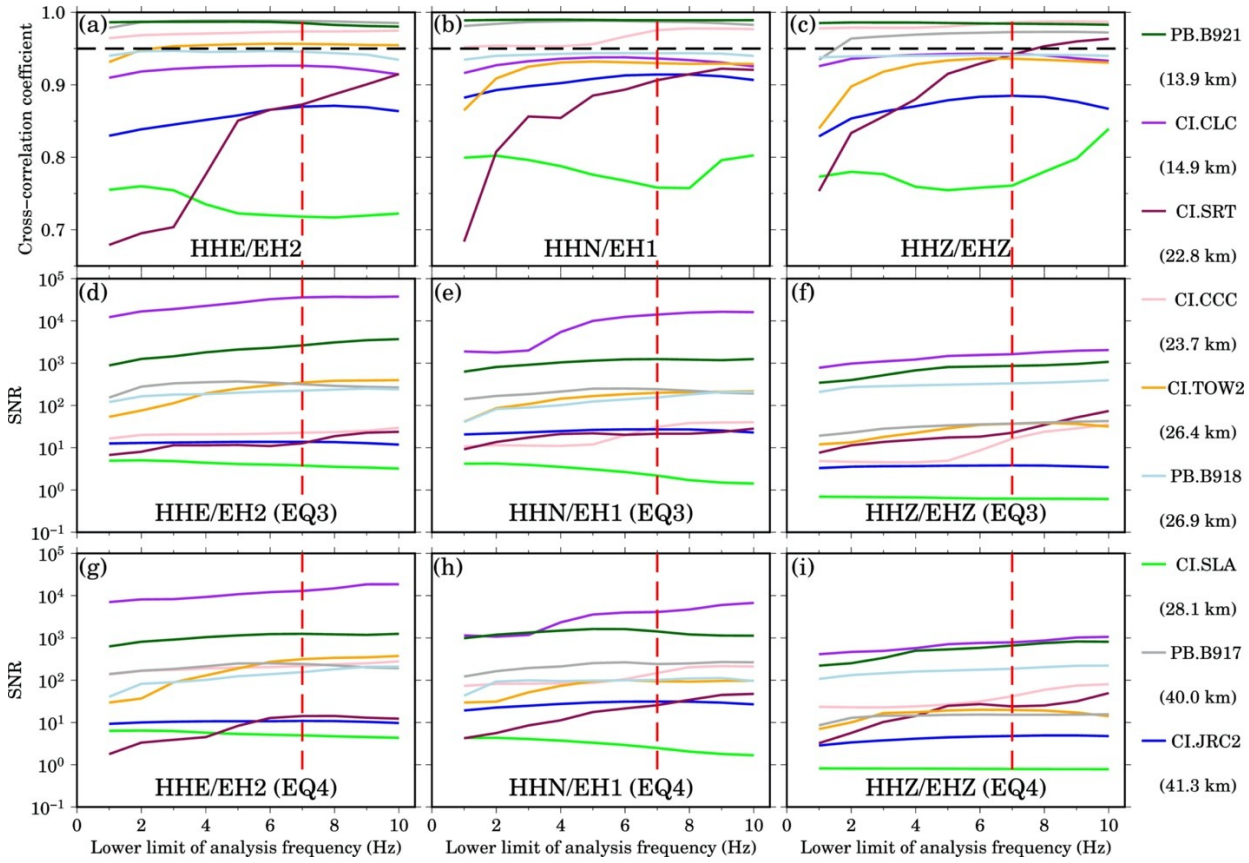

Figure 9. (a) Colored lines represent cross-correlation coefficients of EQs 3 and 4 on HHE/EH2 components with change of the lower limit of analysis frequency (1-10 Hz). The high frequency bound is kept at 25 Hz for all cases. Correspoding station names and their epicenter distances are shown on the right. Black and red dashed lines indicate thresholds of cross-correlation coefficient that used for identifying REs and lower limit of analysis frequency for estimating waveform similarity and coherence, respectively. (b) Similar to (a), but for HHN/EH1 components. (c) Similar to (a), but for HHZ/EHZ components. (d-f) Similar to (a-c), but for SNR analysis of EQ 3 at all stations. (g-i) Similar to (a-c), but for SNR analysis of EQ 4 at all stations.

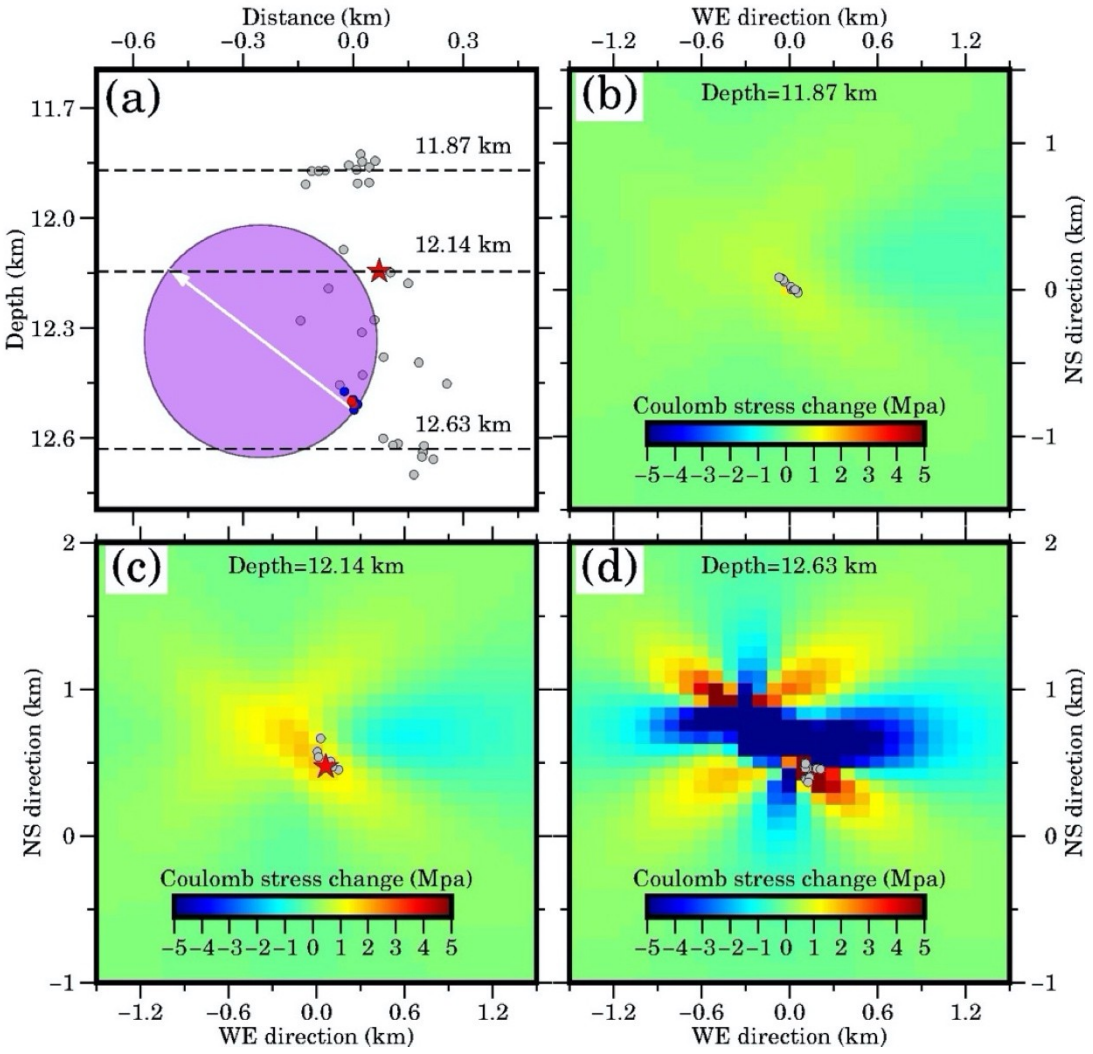

Figure 10. Map demonstrating the nucleation mechanism of the Mw 6.4 mainshock. (a) Cross-section of foreshock distribution along the rupture direction of the M_L 4.0 event shown in Figure 7a. The white arrow marks the initial and end rupture points of the M_L 4.0 foreshock from Figure 7, forming its possible rupture area (transparent purple circle). Gray dots in (a) represent the hypocenters of 32 events that occurred after the M_L 4.0 event and before the Mw 6.4 mainshock along with seven earthquakes (blue dots) that occurred before the M_L 4.0 event. The EQs 3 and 4 are further denoted by red dots. Three black dashed lines mark the depths shown in (b-d). (b-d) Coulomb stress changes imparted by the M_L 4.0 earthquake at depths of 11.87, 12.14 and 12.63 km, respectively. Only foreshocks after the M_L 4.0 event are shown and their epicenters (gray dots) are relative to the epicenter of the M_L 1.5 master event. Red stars in figures (a) and (c) denote the epicenter of the initial rupture point of the Mw 6.4 mainshock.